Transient Thermal Behavior of Internal Short-circuit in Lithium Iron Phosphate Battery

Jieqing Zheng[1,2,*], Yiming Xu[1], Xiang Gao[2], Jianming Zheng[1], Hongzhou He[1] and Zhigang Li[2]

[1] Cleaning Combustion and Energy Utilization Research Center of Fujian Province (Jimei University), Xiamen 361021,P.R. China
[2] Department of Mechanical and Aerospace Engineering, The Hong Kong University of Science and Technology, Clear Water Bay, Kowloon, Hong Kong
[*]E-mail: zhjieqing@126.com

Thermal safety is the most important issue in Lithium Iron Phosphate (LiFePO$_4$) battery applications because of the large amount of energy stored inside them and also because of their great sensitivity to the conditions in which these batteries are used. A large part of thermal damages caused by LiFePO$_4$ battery is associated with short circuit. In this paper, a Multi-Scale Multi-Domain model, which has a high calculation speed and relatively accurate results to quickly respond to the instantaneous thermal abuse condition, is developed to predict internal short circuit (ISC) thermal behaviors of commercial LiFePO$_4$ battery during a discharging process. An 8-order polynomial fitting parameter for function U and a 5-order one for function Y are employed in this model. Also, cell pouch of the LiFePO$_4$ battery as a thickness thermal resistance which has a natural convection boundary condition is taken into account. Simulation results on positive electrode voltage and temperature performances show good agreement with the experimental data. The influences of short-circuit position, short-circuit resistance and discharge rate on the maximum temperature of the battery cell shortly after short circuit are investigated, respectively. The duration time right after short circuit happens to reach the maximum temperature on the short-circuit location and the value of the maximum temperature are focused on, respectively. The simulation results show that, the location of short-circuit does affect the value of maximum temperature, but this effect is not obvious; however, the short-circuit resistance has obvious influence on the time and the value of the maximum temperature at the short-circuit spot; additionally, the effect of discharge rate on the value of maximum temperature shows a linear downward trend, the smaller the short-circuit resistance value is, the greater the slope of the curve is.

1. INTRODUCTION

Lithium ion batteries are high-density carriers of energy. The underlying reason for safety problems therewith is that thermal runaway occurs in batteries and heat constantly accumulates, thus

leading to a continuously increasing temperature in such batteries, which is manifest as a violent energy release in the form of either combustion or explosion. In comparison with other positive electrode materials, due to the solid P-O bond in lithium iron phosphate (LiFePO$_4$) crystals, heating induced by structural collapse does not tend to occur or strong oxidising materials are not easily formed at high temperatures [1-4]. In addition, because of progress in the technology used for insulating ceramic-coated separators, lithium ion batteries are relatively safe. However, internal short circuits (ISC) in battery cells remain the commonest fault and source of potential danger. In practice, there are reports that a small number of samples often combust in nail penetration or short circuit tests. Such a phenomenon has been a problem for lithium ion batteries for more than 20 years, and some product recalls of batteries, and accidents, keep the public worrying about the overall safety of lithium ion batteries.

Therefore, in the development of lithium ion batteries, it is necessary to investigate short circuit problems. Experimentally, representative achievements include the studies conducted by H. Maleki and J.N.Howard [5] in Motorola's laboratory in 2009 and W. Cai, H. Wang, H. Maleki and J. Howard [6] in Oak Ridge State Laboratory in the USA in 2011. They induced ISC in batteries by knocking cylindrical nails into batteries or extruding the upper and lower surfaces of square batteries with two balls to produce physical deformation. Based on this, they studied the effects of many parameters, such as the diameter of the nails, nailing or extrusion speed, nail penetration position, discharge rate, and depth of discharge on changes in temperature and shape of a battery of specific dimensions and capacity. The experiment shows that more than 70% of the stored energy can be released within 60 s after the occurrence of a short circuit. The risks of thermal runaway are determined by three aspects: (1) local heat generation capacity at nail penetration points and event duration, (2) shrinkage, melting point, and diffusion ability of separators, and (3) overall temperature rise in the battery. So far, although many experimental items of equipment and methods for testing short circuits in batteries have been developed, the underlying mechanisms of thermal behavior seen due to short-circuit failure in batteries cannot be completely revealed and elaborated through some specific experimental observation and analysis. The reasons are that the risks of short-circuit experimentation are uncontrollable and a short dot is difficult to create artificially in finished batteries. Therefore, it is necessary to develop the mathematical model for thermal analysis of lithium batteries and replace experimentation with numerical simulation. The equivalent circuit model (ECM), as the simplest mathematical model of ISC, can be used to roughly estimate heat generation rates at short-circuit resistance. In other words, when the short-circuit resistance equals the internal resistance of a battery cell, the rate of heat generation is maximized. However, when the temperature rise in battery cells is large, the corresponding changes of internal resistance cannot be neglected, so this model is not suitable for simulating temperature fields under short-circuit conditions [7]. Electrochemical reaction and heat transfer in batteries are phenomena of multi-scale multi-physical field coupling and can be analyzed from conservation of electrochemical composition and charge conservation (concentration field and electric field) considerations of microcosmic active materials. Then, accurate electric current density, electrode voltages, and temperature distributions in batteries can be obtained by establishing macroscopic mathematical simulation models of momentum and energy conservation (flow field and temperature field) [8-11]. When being used for analyzing a short circuit in a battery, the model can

explain the mechanisms of thermal runaway caused by short circuits between copper and aluminium current collectors, between carbon negative electrodes and aluminium current collectors, between copper current collectors and positive electrode materials, as well as between positive and negative electrode materials. This provides supports for the structural design of batteries and selecting materials based on their thermos-physical behavior mechanisms [12, 13].

Multiple layers in a battery show disadvantages including model complexity and many computations in its simulation. In addition, multiple repeat structures (sandwich structures) repeatedly appear in the battery. For these reasons, it is unnecessary to construct a complete multi-level model for simulation and calculation of overall electrochemical performance of batteries. More importantly, once a short circuit occurs in a battery, thermal runaway is more likely to be instantaneous. At this moment, any thermal management system is required to obtain rapid feedback and make a timeous decisions. It is, therefore, not realistic to build the actual complete model of batteries in engineering applications, so a fast, relatively accurate, calculation model is needed to solve the aforementioned problems. The simplified model (NTGK) jointly developed by Newman, Tiedemann, Gu and Kim [14-18] was used in this study. The semi-empirical mathematical model fitted electrochemical parameters needed by the model through the measured charge-discharge data of a specific battery. The internal structure of the battery cell was simplified into a positive electrode, a separator, and a negative electrode, so as to realize multi-scale multi-domain (MSMD) simulation of active particles, electrodes, and the battery cell. Furthermore, an outstanding problem of an LiFePO$_4$ battery is the inconsistency between products, so the NTGK model, depending on experimental data, can solve this problem.

2. MATHEMATICAL PHYSICAL MODEL
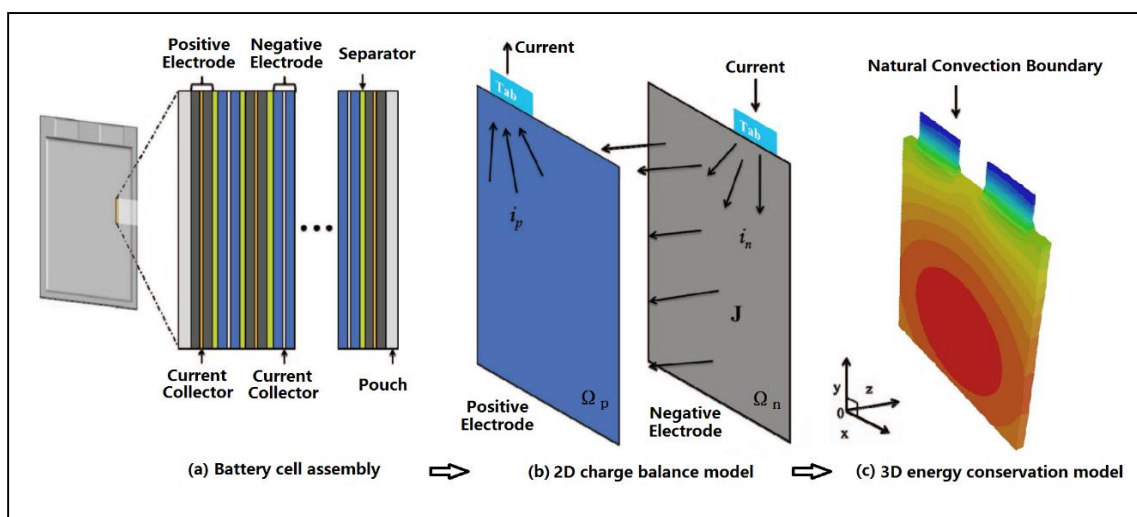
Figure 1. Schematic diagrams of modeling procedure of an LiFePO$_4$ battery cell consisting of multiple alternating layers [19].

The internal structure of a single LiFePO$_4$ battery comprises multiple layers of positive and negative electrodes, separators, positive and negative electrode current collectors, and solid-state

polymer electrolyte individually made with the same shapes and structures. The outer layer of the battery cell was packaged with aluminium-plastic composite film. Of them, the positive electrode material was LiFePO4 which was smeared onto both sides of the aluminium current collector, while graphite was used as the negative electrode and was smeared onto both sides of the copper current collector, separately. A porous separator was placed between positive and negative electrodes, as shown in Fig. 1(a) [19]. Although the internal shape of the battery cell had a 3D structure, charge-discharge flow of currents of each electrode pair appeared as a 2D sandwich structure. It is time consuming to establish a mathematical model of the electrical field with the same, repeated complete structure, so the whole battery cell was simplified as one only consisting of a pair of positive and negative electrodes, as demonstrated in Fig. 1(b) [19]. Moreover, the electrical field parameters were obtained by invoking the charge conservation equation. Finally, by using a CFD method, the 3D mathematical model of the temperature field was built, as displayed in Fig. 1(c), thus coupling the electrical, and temperature, fields.

2.1 Thermodynamic model

In Fig. 1(c), the energy conservation equation (namely, the 3D differential equation of heat conduction) for the whole battery is:

$$\frac{\partial \rho C_p T}{\partial t} = \nabla \cdot (\lambda \nabla T) + \dot{q} \tag{1}$$

Where ρ denotes the density, C_p the specific heat capacity at constant pressure, T the thermodynamic temperature (K), t the time, λ the thermal conductivity, $\dot{q}$ the volumetric heat generation rate ($W \cdot m^{-3}$) of the battery cell, respectively.

Definite conditions of Equation (1) are:

Initial conditions:　　$t = 0, T = T_{amb}$

Boundary condition: $-\lambda \frac{\partial T}{\partial n}\bigg|_w = h(T - T_{amb})$

Where T_{amb} denotes the ambient temperature, h the convective heat transfer coefficient, and $n = x, y, z$ respectively.

Assuming that there is no concentration difference in the battery, the heat generation rate $\dot{q}$ in Equation (1) includes three parts [20]: (1) Irreversible Ohmic heat generation (or known as Joule heating) released in the process of overcoming internal resistance of the battery when charges migrate between positive and negative electrodes; (2) heat generation in the electrochemical reaction; and (3) Irreversible Ohmic heat generation due to battery internal short-circuit. The expression thereof given by:

$$\dot{q} = \sigma_p \left| \nabla V_p^2 \right| + \sigma_n \left| \nabla V_n^2 \right| + \dot{q}_{ech} + \dot{q}_{short} \tag{2}$$

where σ_p and σ_n are the effective electric conductivities ($S \cdot m^{-1}$) for the positive and negative electrodes, V_p and V_n are the phase potentials (V) for the positive and negative electrodes, respectively, and the first and two items on the right side of the equation denote the volumetric Ohmic

heat generation rate of the positive and negative electrodes, the third and fourth terms denote the volumetric heat generation rate due to electrochemical reaction and internal short circuit, respectively.

2.2 Electric field model

In Fig. 1(b), based on charge conservation of the battery in discharge, the following Poisson's equation of positive and negative electrode potentials is established:

$$\nabla \cdot \left(\sigma_p \nabla V_p \right)\Big|_{\Omega_p} = -\left(j_{ech} - j_{short} \right)$$
$$\nabla \cdot \left(\sigma_n \nabla V_n \right)\Big|_{\Omega_n} = j_{ech} - j_{short} \tag{3}$$

Where the subscripts Ω_p and Ω_n represent the computational domains of the positive and negative electrodes, respectively, and j_{ech} and j_{short} denote volumetric current transfer rate ($A \cdot m^{-3}$) due to electrochemical reaction and battery internal short-circuit, respectively.

Definite conditions of Equation (3) are:

$$\frac{\partial V_p}{\partial n}\Big|\Gamma_{p1} = 0, \qquad \frac{\partial V_p}{\partial n}\Big|\Gamma_{p2} = \sigma_p I_0$$
$$\frac{\partial V_n}{\partial n}\Big|\Gamma_{n1} = 0, \qquad \frac{\partial V_n}{\partial n}\Big|\Gamma_{n2} = 0 \tag{4}$$

Where Γ denotes the boundary, the subscripts p_1 and n_1 denote positive and negative boundary, p_2 and n_2 denote the positive and negative electrodes as well as corresponding tab boundaries, respectively. I_0 stands for the total current flowing through the tab under constant-current discharge mode.

In Equation (3), the volume current density j_{ech} is the function of potential difference $\left(V_p - V_n \right)$ of positive and negative electrodes of the battery and depends on the polarization characteristics of the electrodes. Here, the expression recommended by Newman, Tiedemann, Gu and Kim [18, 19] is used:

$$j_{ech} = \alpha Y (U - V_p - V_n) \tag{5}$$

Where α denotes the specific area (m^2/m^3) of the electrode sandwich sheet in the battery cell. Model parameters Y and U denote the empirical fitting functions of depth of discharge DOD of the battery and their polynomial functions are given by:

$$Y = \left[\sum_{i=0}^{n} a_i (DOD)^i \right] \exp\left[-c_1 \left(\frac{1}{T} - \frac{1}{T_{ref}} \right) \right] \tag{6}$$

$$U = \left[\sum_{i=0}^{n} b_i (DOD)^i \right] - c_2 (T - T_{ref}) \tag{7}$$

In Equations (6) and (7), a_i and b_i are constant terms for fitting the polynomial, while c_1 and c_2 represent the constant terms of the NTGK model. For a given battery, the voltage-current response curve can be obtained through experimentation. The expression for DOD is:

$$DOD = \frac{VOL}{3600 Q_{Ah}} \left(\int_0^t j \, dt \right) \tag{8}$$

Where *VOL* denotes the battery volume, and Q_{Ah} is the battery total electric capacity in Ampere hours.

2.3 Short-circuit model

In normal use of the battery, the positive and negative electrodes are separated by a separator, so as to prevent short circuiting due to electrons directly migrating from the negative electrode to the positive electrode by passing through the separator. When the battery is penetrated or extruded, the separator is easily fractured and damaged. Besides that, the battery provides normal current j_{ech}, secondary current produced in electrochemical reactions also occurs in short-circuit regions. In other words, the strength of j_{short} in Equation (3) can be simulated and characterized by using the contact resistance (r_c / α) of variable volume.

$$j_{short} = \alpha(V_p - V_n) / r_c \qquad (9)$$

Where, r_c indicates the contact resistance of area ($\Omega \cdot m^2$). The rate of volumetric heat generation by the short-circuit current in Equation (2) can be expressed as:

$$\dot{q}_{short} = \alpha(V_p - V_n)^2 / r_c \qquad (10)$$

By introducing Bernardi volumetric heat generation model[21], the term $\dot{q}_{ech}$ of normal heat generation rate of current in Equation (2) is expressed as the sum of the irreversible heat generation of polarization resistance and entropy production of a reversible chemical reaction, that is:

$$\dot{q}_{ech} = j_{ech}\left[U - (V_p - V_n) - T \frac{dU}{dT} \right] \qquad (11)$$

Finally, the thermodynamic Equation (1), and Poisson's Equation (3) of the electrical field can be coupled and calculated through the use of Equations (2), (10), and (11).

2.4 Model parameters
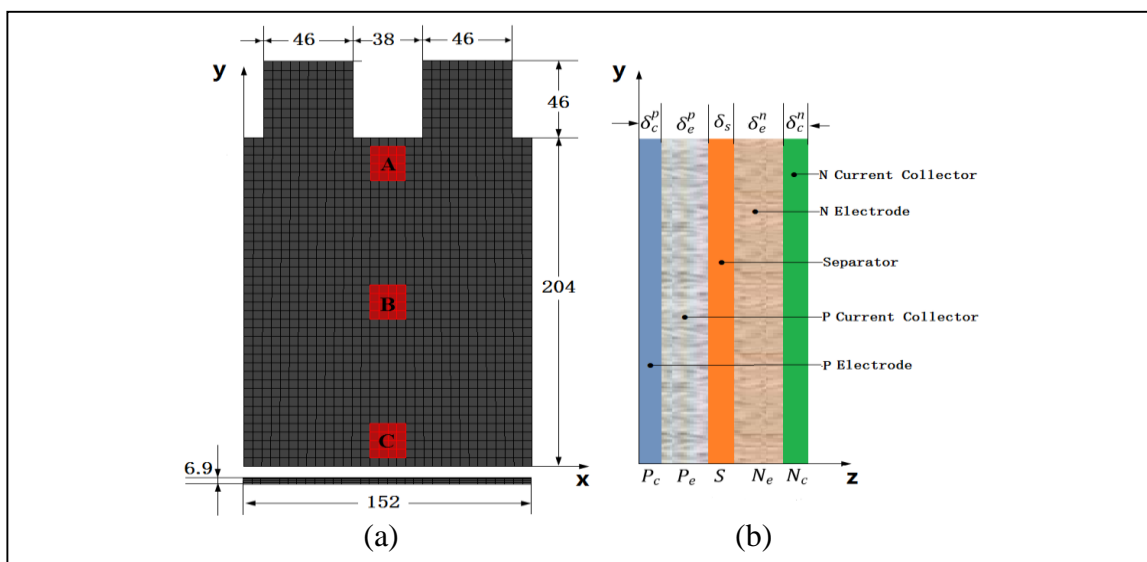
Figure 2. 3D LiFeO₄ battery geometrical dimensions and 2D sandwich structure diagram： (a) geometrical and computing mesh and (b) sandwich sheet.

In this study, an LiFePO4 power battery with the capacity of 20 Ah produced by a brand in the USA for commercial use was used as the research object. Fig. 2 shows its 3D geometrical dimensions and associated computational model mesh. The mesh was formed by regular hexagons and included 4,128 elements and 5,852 nodes. Fig. 2(b) shows a single sandwich sheet in the battery cell. P_c, P_e, S, N_e and N_c represent the positive electrode current collector, positive electrode, separator, negative electrode and negative electrode current collector, respectively. δ_c^p, δ_e^p, δ_s, δ_e^n and δ_c^n denote the thicknesses of each part of the sandwich sheet of the battery cell, respectively.

In the simulation, the following Equations (12) and (13) are used for calculating the total equivalent thickness δ_{total} and the effective property value of a material property x_{eff} (such as density, heat capacity, or thermal conductivity) [22], respectively.

$$\delta_{total} = 0.5\delta_c^p + \delta_c^e + \delta_s + \delta_e^n + 0.5\delta_c^p \qquad (12)$$

$$x_{eff} = \frac{0.5x_c^p\delta_c^p + x_c^e\delta_c^e + x_s\delta_s + x_e^n\delta_e^n + 0.5x_c^p\delta_c^p}{\delta_{total}} \qquad (13)$$

Where, x_c^p, x_e^p, x_s, x_e^n and x_c^n indicate physical parameters of each part of the sandwich sheet, respectively. Additionally, for the electric conductivity σ_p and σ_n:

$$\sigma_p = \frac{0.5\sigma_c^p\delta_c^p + \sigma_e^p\delta_e^p}{\delta_{total}}$$

$$\sigma_n = \frac{0.5\sigma_c^n\delta_c^n + \sigma_e^n\delta_e^n}{\delta_{total}} \qquad (14)$$

The calculation results of Equations (12), (13) and (14) are shown in TableI.

Table I. List of battery parameters used in the model [23- 25].

Zone	Pc(Al)	Pe	S	Ne	Nc(Cu)	Total
Thickness δ [μm]	20	82	12	90	10	199
Density ρ [kg·m^{-3}]	2700	1500	900	2223	8700	2032
Heat capacity C_p [J·kg^{-1}·K^{-1}]	897	800	1883	641	396	788
Heat conductivity λ [W·m^{-1}·K^{-1}]	237	1.48	0.5	1.04	398	23
Electrical Conductivity σ [S·m^{-1}]	3.83E+07	1	-	120	6.33E+07	σ_p 1.92E+06 σ_n 1.59E+06

$*T_{ref} = 300K$

Model fitting parameters in Equations (6) and (7) are presented in Table II and the calculation method for fitting parameters is shown elsewhere [18, 26]. In general, a 3- or 5-order polynomial is

used for fitting function U [19, 22]. In this study, to obtain a more accurate model, an 8-order polynomial is used for fitting, while a 5-order polynomial is used for fitting function Y.

Table II. Fitting parameters used to calculate the potential distributions on the electrodes.

i	0	1	2	3	4	5	6	7	8
a_i	788.6	2826.4	13878.7	27538.5	22696.1	6410.5	-	-	-
b_i	3.49	-7.51	89.77	-521.6	1650.71	2994.41	3093.63	1680.21	368.13
c_i	-	1800	0.095	-	-	-	-	-	-

$^* T_{ref} = 300K$

In Fig. 2(a), red regions A, B, and C demonstrate ISC occurs at three different locations and the volume of the three regions is the same（20μm*20μm*6.9μm）. In the calculation, the method for setting different ISC resistances at each location (A, B, and C) mentioned above is used for adjusting the short-circuit current.

Furthermore, the aluminium-plastic composite film for packing the battery was made of PA/AL/CPP. In the calculation, the film is equivalent to a wall thermal resistor with a thickness of 0.15 mm and a thermal conductivity $\lambda = 20\,W \cdot m^{-1} \cdot K^{-1}$. The ambient temperature of the battery is 300 K (taken as its initial temperature). The natural convection heat transfer coefficient between the battery shell and environment is $h = 5\,W \cdot m^{-2} \cdot K^{-1}$.

2.5 Model verification
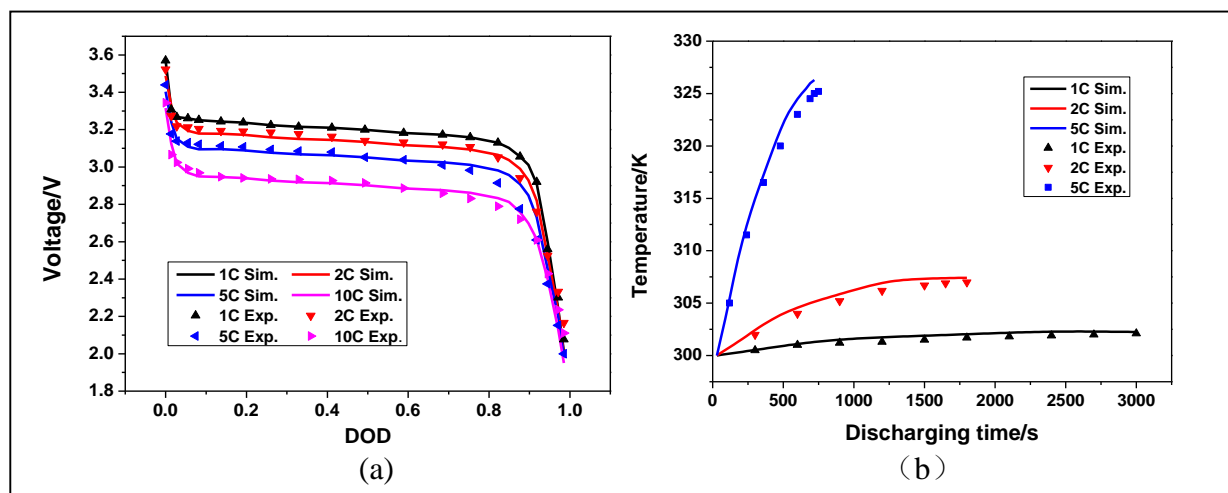
Figure 3. Validation between simulation and experimental data: (a) voltage and (b) temperature.

On the NEWARE BTS-5V200A charge-discharge test platform, the battery was charged to 3.6 V at constant current (20 A) and constant voltage and stood for 2 h, consequently. After that, the battery was discharged to 2 V at discharge rates of 1 C, 2 C, 5 C, and 10 C, respectively. In the discharge process, the temperature of central point on the surface of the LiFePO$_4$ battery was measured in real time by using a temperature sensor. The experiment and simulation results of voltage and temperature changes are shown in Fig. 3. The comparison of data demonstrates that in the earlier stage of discharge or at the lower discharge rate, simulated values of both the voltage and temperature curves matched the experimental data very well, while in the later stage or at the higher discharge rate, simulated values showed certain deviations therefrom. The following three aspects were considered to be the error sources of the model: (1) to highlight characteristics of thermal behaviors at the moment of the short circuit in the discharge, the calculation model built in the study does not take contact resistance of positive and negative tabs into account; (2) only natural convection heat dissipation between the battery shell and the environment is considered, while heat dissipation due to radiation is not taken into account; (3) the error from fitting itself is an inevitable system error. On the whole, the maximum deviations in simulated values of voltage and temperature in the range of measured data were 4.3% and 4.6%. Therefore, it is considered that the 3D mathematical model established in this study accurately reflects the thermal behavior of the battery.

3. RESULTS AND DISCUSSION
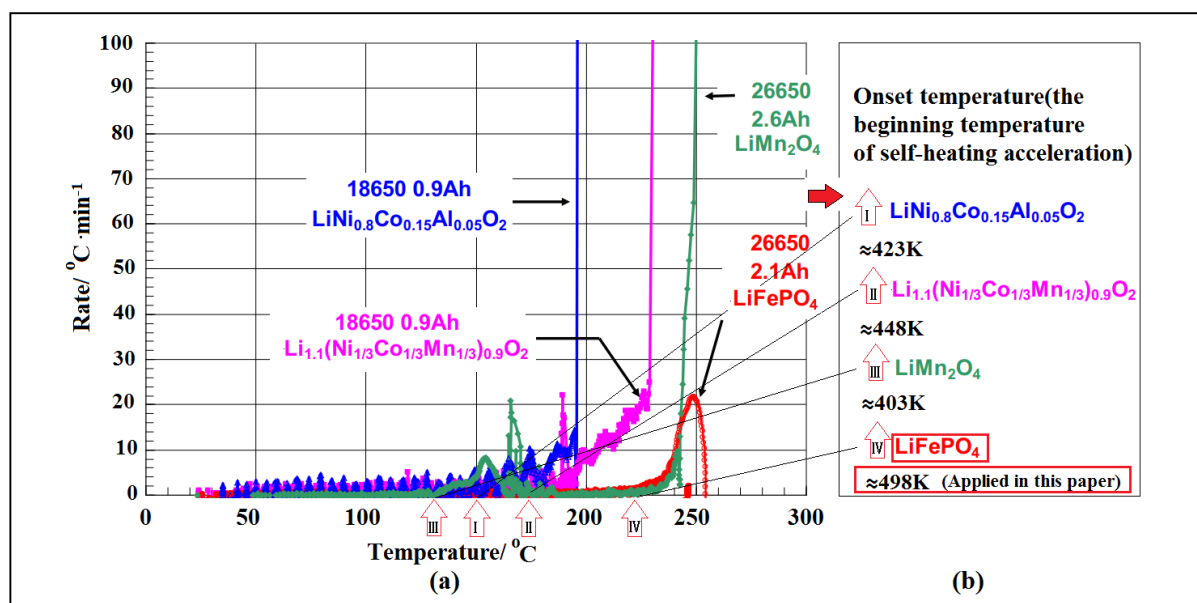
Figure 4. Onset temperature of LiFePO$_4$ applied in the simulation: (a) onset of self-heating in thermal ramp experiment on Li-ion cells [27] and (b) the beginning temperatures of self-heating acceleration for different types of battery chemistries.

Due to the limitations of the model, after the temperature rose to a certain value, some undesirable intense chemical reactions and self-heating behaviors occurring in the battery could not be simulated. Therefore, the short treatment in the model places a special emphasis on predicting the

thermal ramp-up process before the onset of thermal runaway, so as to timeously warn of, and control, failure in the thermal management system of the battery. Firstly, therefore, the transition temperature at the beginning of self-heating acceleration should be set to break off during the simulation.

The literature [12] shows that the transition or onset temperature for self-heating of a $LiCoO_2$ lithium battery appeared in the temperature range of 473 K to 483 K. However, the $LiFeO_4$ battery is more resistant to thermal runaway and then has a higher onset temperature [2, 27-30]. D. Doughty and E.P. Roth [27] figured out the thermal ramp-up profiles of $LiNi_{0.8}Co_{0.15}Al_{0.05}O_2$, $Li_{1.1}(Ni_{1/3}Co_{1/3}Mn_{1/3})_{0.9}O_2$, $LiMn_2O_4$ and $LiFePO_4$ batteries before and after self-heating acceleration, respectively(see Fig.4 (a)). The result is basically consistent with the literatures [2, 28-30]. In this study, therefore, once the maximum temperature exceeds 498 K (red, see Fig.4 (b)) during simulation, the battery is considered to be in danger of thermal abuse, and special protection should be required promptly. Generally, the approach developed in this paper could be applied to other types of battery chemistries, simply by modifying the onset temperature as indicated in Fig.4.

3.1 Internal short-circuit location

Owing to local large currents passing through the system, heat that could not be released accumulated at the short-circuit location, rapidly increased the local temperature. Fig.5 shows the calculated temperature distribution when an ISC occurred at A, B, or C in the battery within 5 s under conditions that the discharge rate and short circuit resistance are 1 C and $1\,\mu\Omega$, respectively.
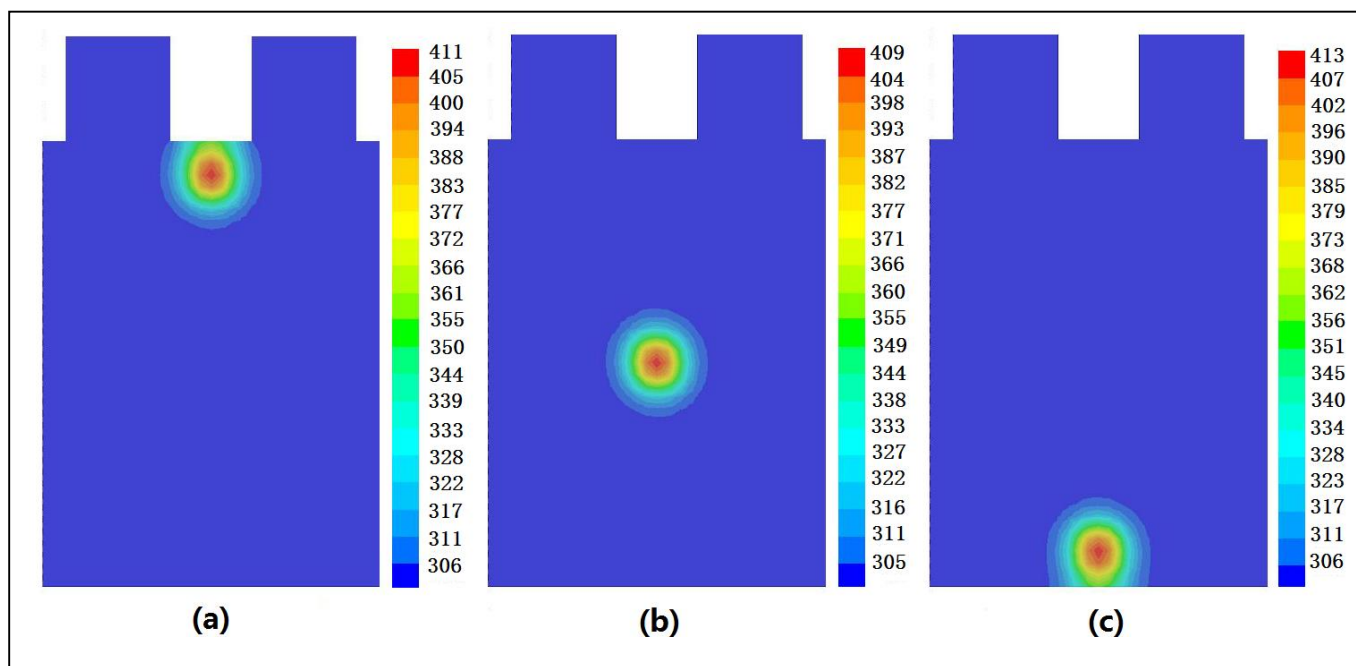
Figure 5. Simulated temperature distributions with ISC locations in the (a) middle of the top, (b) center and (c) middle of the bottom of the battery cell with a discharge rate of 1C and an ISC resistant of 1 μΩ at a discharge time of 5 s.

As shown in the Fig.5, the local maximum temperature at short-circuit position represented the overall maximum temperature of the battery. Within 5 s, the local maximum temperature of the battery exceeded 400 K, and thermal runaway was about to occur. When the short circuit appeared at central location B, the temperature rose at the slowest rate to the maximum temperature of 409 K, followed by that at A (the maximum temperature being 411 K), while the temperature rise rate in the bottom location C was the fastest (the maximum temperature being 413 K). Heat in local areas was dissipated through three methods, that is, heat conduction to the surroundings, natural convection, and thermal radiation to the environment. In comparison, because of the low natural conversion and heat transfer coefficient (being 5 to 20 but set to 5 in this study) and small radiation temperature difference (the model used here did not consider heat dissipation induced by radiation), only a limited amount of heat was transferred by using the above two methods and heat conduction to the surroundings was the main method of heat dissipation. Heat in the middle location B was more easily transferred to the surroundings by heat conduction and the heat dissipation conditions in the center of the bottom were the worst. While the center of the top showed similar heat dissipation conditions to those at the bottom, it had better heat dissipation conditions than the bottom owing to it being closer to the tab. Although this study did not analyze short circuits in other locations, it may be inferred that the worst results were more likely to appear on both sides of the bottom.

3.2 Internal short-circuit resistance
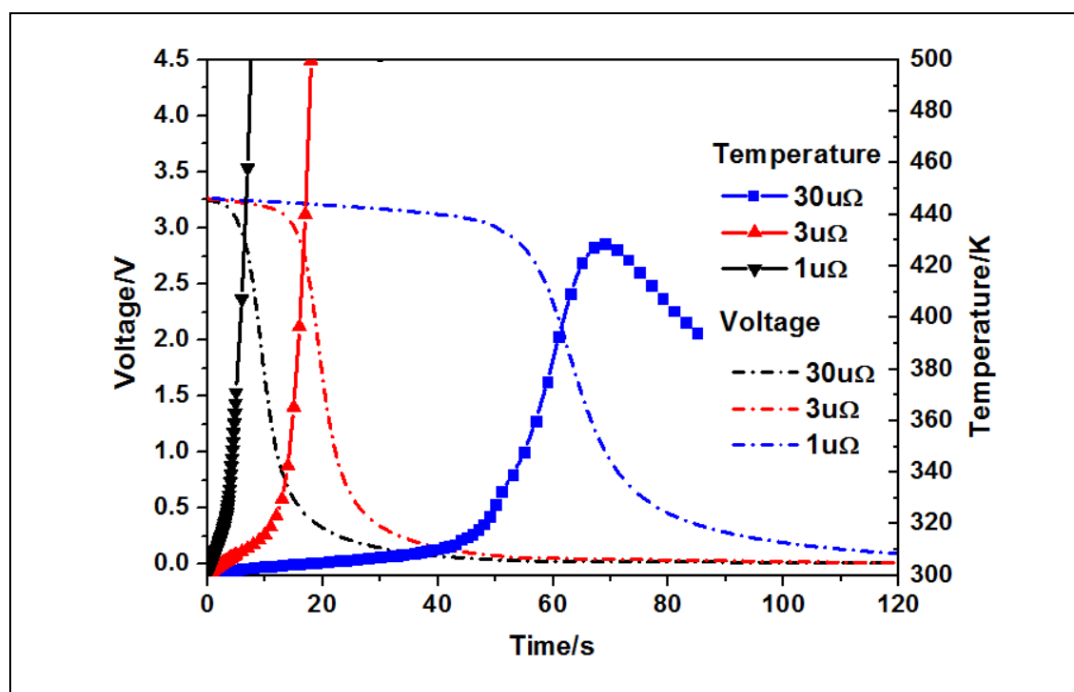
Figure 6. Simulated maximum temperature, and voltage, response curves with a discharge rate of 1 C under the ISC resistances of 1, 3 and 30 μΩ located in the center of the battery cell.

In the current discharge at 1 C, Fig.6 shows the change curves of positive potential (the potential of the negative electrode is 0) and the local maximum temperature of short-circuit position in

the center of the battery with discharge time when discharge rate is 1 C and short-circuit resistances are 1, 3, and 30 μΩ. When the short circuit resistance was 1 and 3 μΩ, heat generated by the short-circuit resistance, when a large current was passed through rapidly, accumulated and could not be quickly dissipated to the surroundings. As a result, the temperature of the battery rapidly exceeded 498 K at 21 s after discharge and correspondingly the voltage quickly decreased to near-zero within 40 s, however, when the short-circuit resistance increased by one order of magnitude, for example at 30 μΩ as shown in Fig. 6, voltage showed a gentle decrease process for about 50 s and then began a rapid decrease lasting for 30 s. After 80 s, the voltage began to decrease slowly to zero. The concentrated release of energy was much slower than that in the two aforementioned conditions, so that Ohmic heat generated from short-circuit current had relatively enough time to be dissipated to the surroundings and environment, and therefore, the temperature of the local short-circuit location did not rise to the maximum (430 K) until a 70-s delay. After that, owing to the rate of heat generation being smaller than the rate of heat dissipation, the temperature rapidly decreased from the maximum.

During the discharge of the battery, the short-circuit process was divided into the early, middle, and late stages according to the change in voltage. Firstly, voltages in the early and late stages decreased gradually. The corresponding temperature changes showed two distinct trends: (1) In the early stage of the discharge, heat slowly accumulated and the temperature increased slowly. (2) In the late stage, too high a temperature gradient in the local area strengthened the temperature equalization effect and promoted rapid dissipation of heat, so that the phenomenon of too high a temperature in local areas could be quickly relieved and the temperature decreased. In the middle stage of discharge, the voltage decreased rapidly, while the temperature rose rapidly.

Based on the above analysis, it can be seen that the short-circuit resistance affected the transition times between, and durations of, the three stages of discharge. The maximum temperature at the short-circuit location of the battery and its trend after the occurrence of a short circuit were thus indirectly determined.

3.3 Discharge rate

Besides that short-circuit resistance had individual effects on temperature changes, Fig. 7 shows the influence of different short-circuit resistances and discharge rates on the maximum temperature of local short-circuit locations in the center of the battery shortly after the short circuit. In the simulation and calculation, the discharge occurs at 5 s and the short-circuit resistances are set to 0.5, 0.7, 1, and 3 μΩ, separately. Moreover, discharge rates are set to 0.5, 1, 2, 3, 5, and 10 C, respectively (see Fig. 7).
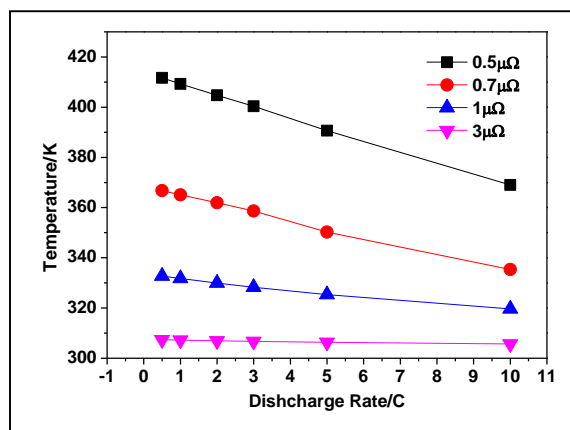
Figure 7. Impact of different discharge rates on the maximum temperatures under the ISC resistants of 0.5, 0.7, 1 and 3 μΩ located in the center of the battery cell at a discharge time of 5 s.

Firstly, in comparison with the situation at the same discharge rate and duration, it can be seen that the maximum temperature at the short-circuit location decreases with the increase of short-circuit resistance, which agrees with the conclusions drawn from an inspection of Fig. 6. The underlying reasons have already been analyzed above, so are not described further.

Secondly, under the same short-circuit resistance, the maximum temperature of short-circuit locations follows a quasi-linear decreasing trend with an increasing discharge rate. To ascertain why, Fig. 8 shows the change in total heat generation rate and three parts of the rate of change in the battery after 5 s of discharge under the influences of different discharge rates when the short-circuit resistance is 0.5 μΩ. The three parts of the heat generation pattern include the Ohmic heat generation rate of the short-circuit current, the heat generation rate of the electrochemical reaction, and the Ohmic volumetric heat generation rate, as shown in Equation (2). As can be seen in Fig. 8, the three parts are ranked thus: heat generation in the electrochemical reaction, Ohmic heat generation rate from the short-circuit current, and Ohmic volumetric heat generation. Of them, the heat generation rate of the electrochemical reaction accounts for about 80%, and Ohmic heat generation from the short-circuit current accounts for about 20%, of the total heat generation, however, the proportion of Ohmic volumetric heat generation is no more than 1% overall. When the discharge rate was increased, Ohmic heat generation from the short-circuit current remained unchanged. Although the rate of irreversible Ohmic volumetric heat generation increased constantly, heat generation rate in the electrochemical reaction decreased. Owing to the Ohmic volumetric heat generation rate accounting for a small proportion overall, the changes in total heat generation rate in the battery are mainly affected by the rate of heat generation from the electrochemical reaction. Therefore, the total heat generation rate shows a decreasing trend over a very short discharge time. This allows more heat accumulated in the short-circuit location to be transferred to the surroundings at a high discharge rate. At a high discharge rate, therefore, the maximum temperature decreases.
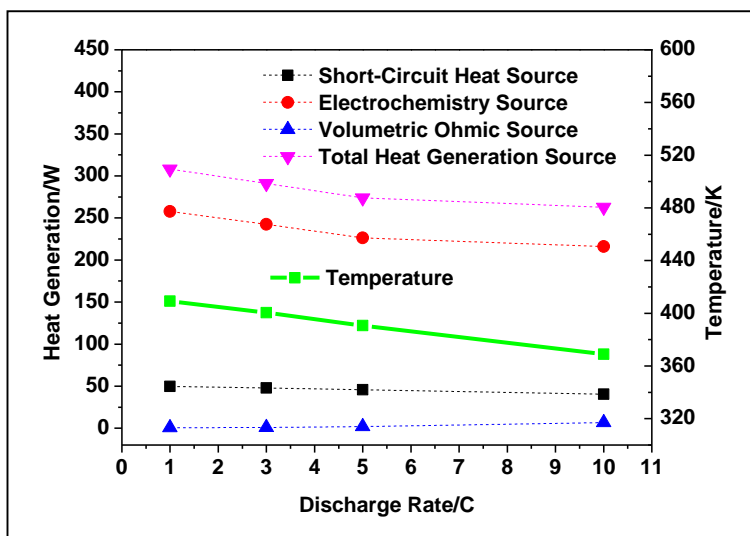
Figure 8. Impact of discharge rate on the heat generation details and maximum temperatures at a discharge time of 5 s with an ISC resistant of 0.5 $\mu\Omega$ located in the center of the battery cell.

Finally, the approximately linear decreasing trend in the maximum temperature at the short-circuit location with increasing discharge rate gradually diminishes with increasing short-circuit resistance (see Fig. 7). Even after the short-circuit resistance reaches $3\,\mu\Omega$, this decreasing trend was insignificant. By combining these data with those plotted in Fig. 6, this was seen to have been because the discharge process was still in the early stage within 5 s after the short circuit occurred when the short-circuit resistance was large. At this time, the voltage decreases slowly, while little heat is accumulated.

4. CONCLUSIONS

In view of the characteristics of the charge-discharge curve of the LiFePO$_4$ battery, an 8-order, and 5-order, polynomials were used for fitting functions *U* and *Y*, respectively. By considering heat conduction through the thin wall of the battery shell and natural convection and heat dissipation to the outside, the 3D NTGK electrochemical-thermal coupled mathematical model, more confirming to reality, was established. Based on a comparison with experimental data, this model could explain the thermal behaviour at the instant of ISC in the battery. Furthermore, due to the high efficiency of operation, the model is especially suitable for practical engineering application in the thermal safety management system of LiFePO$_4$ batteries.

Once a short circuit occurred in the battery, a lot of heat instantaneously accumulated in the short-circuit location. Compared with natural convection and radiative heat transfer, heat conduction played a decisive role in the diffusion of the heat thus accumulated, and therefore, the closer the short-circuit location to the center of the battery, the better the heat dissipation effects. Nevertheless, the simulated data in this study show that differences in temperature changes were found in different locations but not to any significant extent.

Owing to the short-circuit resistance directly determining the reduction in the positive voltage curve, it played a key role in determining the maximum temperature that the battery could reach after occurrence of a short circuit and how quickly it rose to that temperature. The simulated data show that the battery can reach thermal runaway in about 5 s when the short-circuit resistance was less than 10^{-6} Ω. With the increase in the short-circuit resistance to more than 10^{-6} Ω, the maximum temperature that the battery was able to reach significantly decreased and the time to reach this value was also significantly prolonged.

The influences of discharge rate on Ohmic heat generation rate of short-circuit current can be ignored. Although irreversible Ohmic volumetric heat generation rates constantly rose with the discharge rate, the rate of heat generation from the electrochemical reaction (accounting for about 80% of the total heat generation rate) decreased. Only for those samples of the LiFePO$_4$ battery tested in this study, did the simulated data show that the changes in the total rate of heat generation were mainly affected by the rate of heat generation from the electrochemical reaction under the same short-circuit resistance. Five seconds after the occurrence of a short circuit, the maximum temperature of the battery showed a linear decreasing trend with an increasing discharge rate and such a trend tended to diminish with increasing short-circuit resistance.

References

1. X.M. Xu, J.Q. Fu, H.B. Jiang and H. Ren, *International Journal of Energ Restore*, 41(2017)1642.
2. Y.Y. Yu, J. Wang, P. Zhang and J.B. Zhao, *Journal of Energy Storage*, 12 (2017) 37.
3. T.M. Bandhauer, S. Garimella and T.F. Fullerb, *J. Electrochem. Soc.*, 158 (2011) R1.
4. Z.H. Wang, H.F. Xiang and L.J. Wang, *J. Membr. Sci.*, 553 (2018) 10.
5. H. Maleki and J.N. Howard, *J. Power Sources*, 191 (2009) 568.
6. W. Cai, H. Wang, H. Maleki and J. Howard, *J. Power Sources*, 196 (2011) 7779.
7. W. Fang, P. Ramadass and J.Z. Zhang, *J. Power Sources*, 248 (2014) 1090.
8. J. Li, Y. Cheng, M. Jia, Y. Tang, Y. Lin, Z. Zhang and Y. Liu, *J. Power Sources*, 255 (2014) 130.
9. Y. Ye, Y. Shi and N. Cai, *J. Power Sources*, 199 (2012) 227.
10. Y. Cheng, J. Li, M. Jia, Y.W. Tang, S.L. Du, L.H. Ai, B.H. Yin and L. Ai, *Acta Phys. Sin.*, 64 (2015) 210.
11. S. Du, M. Jia, Y. Cheng, Y. Tang, H. Zhang, L. Ai, K. Zhang and Y. Lai, *International Journal of Thermal Sciences*, 89 (2015) 327.
12. R. Zhao, J. Liu and J. Gu, *Applied Energy*, 173 (2016) 29.
13. S. Santhanagopalan, P. Ramadass and J.Z. Zhang, *J. Power Sources*, 194 (2009) 550.
14. W. B. Gu and C.Y. Wang, *J. Electrochem. Soc.*, 147 (2000) 2910.
15. J. Newman and W. Tiedemann, *J. Electrochem. Soc.*, 140 (1993) 1961.
16. H. Gu, *J. Electrochem. Soc.*, 130 (1983) 1459.
17. U.S. Kim, C.B. Shin and C.S. Kim, *J. Power Sources*, 180 (2008) 909.
18. U.S. Kim, J. Yi, C.B. Shin, T. Han and S. Park, *J. Electrochem. Soc.*, 158 (2011) A611.

19. J. Yi, U.S. Kim, C.B. Shin, T. Han and S. Park, *J. Electrochem. Soc.*, 160(2013) A437.
20. V. Srinivasan and C. Y. Wang，*J. Electrochem. Soc.*, 150 (2003) A98.
21. D. Bernardi, E. Pawlikowski and J. Newman, *J. Electrochem. Soc.*, 132 (1985) 5.
22. P. Vyroubal, T. Kazda and J. Maxa, *Int. J. Electrochem. Sci.*, 11 (2016) 1938.
23. Q. Xia, Z. Wang, Y. Ren, B. Sun, D.Z. Yang and Q. Feng, *J. Power Sources*, 386 (2018) 10.
24. A. Samba, N. Omar, H. Gualous, Y. Firouz, P.V.D. Bossche, J.V. Mierlo and T.I. Boubekeur, *Electrochim. Acta*, 117 (2014) 246*.*
25. F.M. Jiang, P. Peng and Y.Q. Sun, *J. Power Sources*, 243 (2013) 181.
26. J. Lee, J. Yi, C.B. Shin, S.H. Yu and W.I. Cho, *Energies*, 6 (2013) 5597.
27. D. Doughty and E.P. Roth, *Electrochem. Soc. Interface*, summer (2012) 37.
28. K. Zaghib, J. Dubé , A. Dallaire, K. Galoustov, A. Guerfi, M. Ramanathan, A. Benmayza, J. Prakash, A. Mauger and C.M. Julien, *J. Power Sources*, 219 (2012) 36.
29. J. Jianga and J.R. Dahnb, *Electrochem. Commun.*, 6 (2004) 39.
30. A.S. Andersson, J.O. Thomas, B. Kalska, and L. Häggström, *Electrochem. Solid-State Lett.*, 3 (2000) 66.